Up-Cycling of Iron-Rich Inorganic Waste in Functional Glass-Ceramics

Acacio Rincón Romero [1], Daniele Desideri [2], Aldo R. Boccaccini [3] and Enrico Bernardo [1,*]

[1] Department of Industrial Engineering, University of Padova, Via Marzolo 9, 35131 Padova, Italy;
   acacio.rinconromero@unipd.it
[2] Department of Industrial Engineering, University of Padova, Via Gradenigo 6/A, 35131 Padova, Italy;
   daniele.desideri@unipd.it
[3] Institute of Biomaterials, Department of Materials Science and Engineering, University of
   Erlangen-Nuremberg, Cauerstraße 6, 91058 Erlangen, Germany; aldo.boccaccini@ww.uni-erlangen.de
* Correspondence: enrico.bernardo@unipd.it; Tel.: +39-049-827-5510

check for updates

Abstract: The intensive mechanical stirring of suspensions of recycled glass and inorganic waste powders in 'weakly alkaline' aqueous solutions (e.g., 2.5–3 NaOH), followed by viscous flow sintering at 800–1000 °C, easily yields highly porous glass-ceramic foams. The firing determines just the consolidation of powders with concurrent incorporation of pollutants from iron-rich waste, such as fly ash from coal combustion (FA). Engineered mixtures allow for the obtainment of chemically stable foams from treatments in air. Treatments in nitrogen are even more significant since they extend the conditions for stabilization and promote novel functionalities. In addition, the change in the atmosphere favors the formation of magnetite (Fe_3O_4), in turn enabling ultra-high dielectric permittivity and semiconductivity. Such a condition was further evidenced by preliminary tests on recycled glass combined with residues from the Bayer processing of aluminum ores or red mud (RM).

Keywords: glass-ceramics; viscous flow sintering; cellular ceramics; alkaline activation; gel casting; electrical functionalities

1. Introduction

Circular economy (CE) can be generally defined as an integrated approach to combat environmental challenges and promote sustainable development [1,2] by systematic reduction of the resources escaping from a product life cycle, e.g., by keeping the added value of the same product for as long as possible and eliminating waste [3]. It obviously includes actions of 'waste recovery' through reuse, recycling, and energy generation.

Industrial inorganic residues, such as fly ash from coal combustion (FA) and residues from the Bayer processing of aluminum ores (red mud (RM)), cannot be excluded from the CE perspective, but they present significant challenges. They are byproducts enriched in pollutants (heavy metal ions), available in very large quantities, and reusable for new products only in specified conditions, combined with other components, and in mixtures destined for the manufacturing of construction materials [4,5].

Among construction materials possibly including fly ash and red mud, a modern solution is represented by 'inorganic polymers' [6–8]. Inorganic polymers can be defined as the products of the dissolution of solid silica- and alumina-rich starting materials in highly concentrated alkali solutions, followed by gelation according to the condensation of corrosion products (hydrated silica- and alumina-based compounds) at near-room temperature. The molecular structure of the gels is highly variable; excellent mechanical properties and chemical stability are typically achieved with the

subgroup of inorganic polymers known as geopolymers, which feature zeolite-like gels [9]. Such gels are determined by the polymerization of SiO_4 and AlO_4 tetrahedral units from the dissolution of starting materials, in the form of a three-dimensional network structure, with alkali ions resulting from the activating solution trapped in the interstitial spaces and stabilizing the tetrahedral coordination of Al ions [9]. It is evident that the formation of a zeolite-like gel corresponds to quite well-defined proportions between silica, alumina, and alkali oxides, which are generally obtained by the use of synthetic alkali silicates and aluminates as alkaline activators instead of simple sodium hydroxide [10].

Discarded glasses, e.g., fractions of common soda-lime glass enriched in heterogeneous contaminants, resulting as a byproduct of the refining of cullet or glass not directly recyclable in the manufacturing of the original articles (such as pharmaceutical glass), have been already introduced for more sustainable geopolymerization of fly ash and red mud coupled with sodium hydroxide [10–13]. However, a possible weakness in the approach is represented by the high hydroxide molarities [14].

The reduction of NaOH molarity ('weak alkali activation') has contrasting effects since it compromises the chemical stability of the products that could be recovered by ceramization of the gels upon treatment at moderate temperatures, i.e., not exceeding 1000 °C. On the one hand, the advantage in sustainability arising from lower NaOH addition is lost with the application of firing treatments. On the other hand, the ceramic transformation brings new opportunities according to the functionalities of the products. As an example, fly ash/soda-lime glass mixtures undergoing activation in weakly alkaline solutions may be used as precursors for highly porous glass-ceramics to be considered for thermal and acoustic insulation [15]. The gelation of suspensions does not constitute a final step but a processing tool. More precisely, suspensions can be foamed simply by intensive mechanical stirring ('frothing') with the help of surfactants, and the viscosity increase associated with the same gelation prevented the collapse of the cellular structures upon drying. The subsequent firing provides a final consolidation by viscous flow sintering.

The present paper is aimed at disclosing further opportunities for the stabilization of coal combustion fly ash, coupled with soda-lime glass, arising from the ceramization of highly porous bodies prepared by the frothing of suspensions in weakly alkaline solution. In particular, treatments in nitrogen, following recent experiences [16], were found to extend the conditions for stabilization and determine novel functionalities, such as ultra-high dielectric permittivity and electrical conductivity, in turn, triggered by the control of magnetite (Fe_3O_4) separation. These results were generalized by preliminary tests involving red mud as key inorganic waste.

2. Materials and Methods

Highly porous bodies were developed using either FA (mean particle size of 20 μm, provided by Steag Power Minerals, Dinslaken, Germany) or RM (<75 μm, provided by Alteo, Gardanne, France) combined with soda-lime glass waste (SLG), corresponding to powders (<30 μm) resulting from purification of glass cullet (SASIL S.r.l., Brusnengo, Biella, Italy). The chemical composition of the starting materials is reported in Table 1.

Table 1. Chemical Composition (expressed in wt.%) of the Starting Materials.

Oxide (wt.%)	SiO$_2$	Al$_2$O$_3$	Na$_2$O	K$_2$O	CaO	MgO	Fe$_2$O$_3$	TiO$_2$
FA	54.36	24.84	0.83	3.03	2.56	2.06	8.28	1.07
SLG	70.50	3.20	12.00	1.00	10.00	2.30	0.42	0.07
RM	5.21	15.21	2.40	0.63	2.95	0.38	52.94	8.05

According to previous experiments [15], FA/SLG powder mixtures in the weight proportions of 76/24, 64/36, and 54/46 (labeled as '5S', '6S', and '7S', owing to a SiO_2/Al_2O_3 theoretical overall molar ratio of 5, 6, and 7, respectively) were cast in a 3M NaOH aqueous solution (solid content of 70%). They were left for 4 h at room temperature under mechanical stirring (500 rpm). RM/SLG powder

mixtures (in the weight proportions of 70/30) were processed similarly, except for lower solid content (65%) and molarity of activator (2.5M NaOH). In both cases, after preliminary mixing, the suspensions were transferred in closed polystyrene containers and placed at 75 °C for 2h. Added later to the suspensions were 4 wt.% Triton X-100 (polyoxyethylene octyl phenyl ether—$C_{14}H_{22}O(C_2H_4O)_n$, n = 9–10, Sigma-Aldrich, Gillingham, UK) surfactant which were foamed by intensive mechanical stirring (2000 rpm) for 10 min. The resulting 'green' foams were then dried at 40 °C for 48 h before being demolded. The foams were finally consolidated by thermal treatment at 700–1000 °C using a heating rate of 5 °C/min and a holding time of 1 h in a flowing nitrogen atmosphere.

The mineralogical analysis was conducted by X-ray diffraction analysis (XRD) on powdered samples (Bruker D8 Advance, Karlsruhe, Germany—CuKα radiation, 0.15418 mm, 40 kV–40 mA, 2θ = 10–70°). The phase identification was performed using the semi-automated Match!$^{\circledR}$ program package (Crystal Impact GbR, Bonn, Germany), supported by data from the PDF-2 database (ICDD-International Centre for Diffraction Data, Newtown Square, PA, USA).

The geometric density was evaluated considering the mass by volume ratio. The apparent and true densities were measured by using a helium pycnometer (Micromeritics AccuPyc 1330, Norcross, GA, USA) on bulk or finely crushed samples, respectively. The three density values were used to compute the amounts of open and closed porosity. Compression tests were done using an Instron 1121 UTS (Instron, Danvers, MA, USA) machine, with a crosshead speed of 0.5 mm/min, employing foam samples of about 10 mm × 10 mm × 10 mm cut from larger specimens. Each data point corresponds to 9–10 samples.

Leaching tests on foams fired in nitrogen were performed based on Norm EN 12457-4 on samples broken into pieces smaller than 4 mm. The pieces were immersed in pure distilled water (liquid/solid ratio = 10) and left for 24 h under mechanical stirring. Suspensions were poured in a smaller flask and centrifuged in order to separate the solid material from the liquid, then later analyzed by means of inductively coupled plasma (ICP; SPECTRO Analytical Instruments GmbH, Kleve, Germany).

The electrical characterization of the materials (FA/SLG and RM/SLG power mixtures) was performed by using disc-shaped samples (diameter of 45–54 mm, thickness of 5–11 mm). The opposite parallel surfaces of the discs were metalized by manual deposition of silver conductive paint (during the painting, the lateral surface was masked with paper tape). An electrical wire was connected to each metalized surfaces by means of a copper tape with conductive adhesive (3M copper foil tape 1181). The equivalent model assumed for the final configuration was an inductance L, due to the wires, in series with the parallel between a resistance R and a capacitance C, due to the sample with metalized parallel surfaces.

A precision LCR meter (GW Instek LCR-6300, frequency range: 10 Hz–300 kHz) was used for the impedance measurements.

Each wire was kept about 0.1 m long, giving an inductance due to the wires of the order of 100 nH. The experimental data reported in this paper are for samples where the inductive contribution of the wires, in the measured frequency range, was negligible with respect to the experimental impedance value and, therefore, the measured impedance was due to the parallel between R and C. An estimation of the electrical resistivity was obtained according to Ohm's law, from the measured R-value and the disc geometry. An estimation of the relative permittivity was derived according to the hypothesis of parallel plate capacitor configuration from the measured C value and the disc geometry.

3. Results and Discussion

3.1. Effect of Firing Atmosphere on Microstructure and Properties of Fly Ash-Derived Glass-Ceramic Foams

The adopted methodology led to highly homogeneous foams from FA/SLG mixtures. As shown by Figure 1, the microstructure was not visibly altered passing from 'green' (Figure 1a,b) to fired state (Figure 1c,d), as observed in a previous investigation concerning the firing in the air [15]. The analogy with foams fired in air involved also the porosity, which remained mostly open, as shown in Table 2.

However, unlike samples fired in the air, treatments at 700 °C did not suffice for consolidation. The samples could be crushed even by gentle hand pressure.
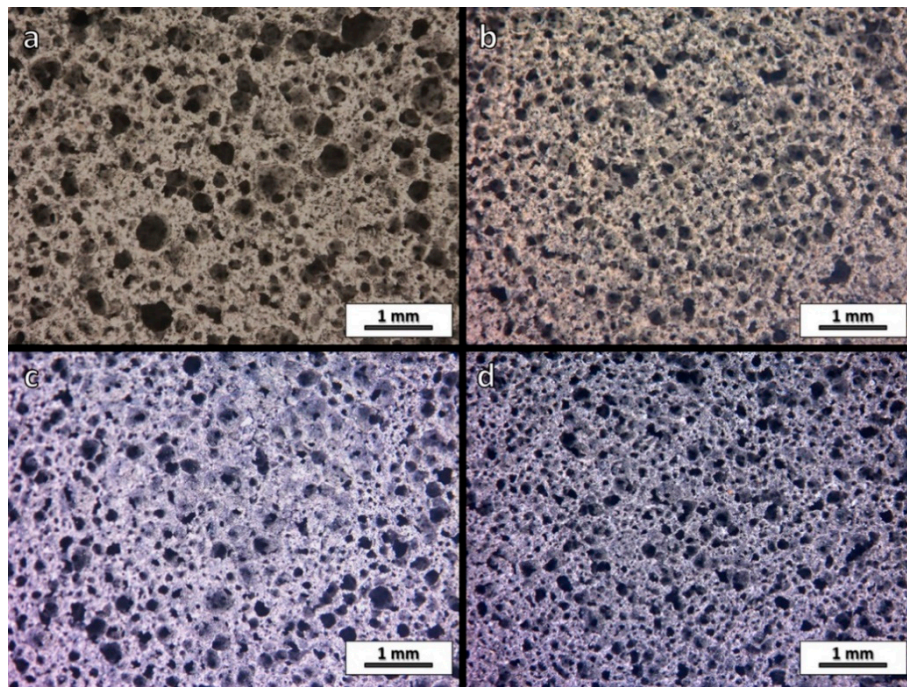
Figure 1. Optical stereomicroscope images of fly ash/glass-derived foams in the 'green' state (**a**): 5S; (**b**): 7S and after firing at 800 °C (**c**): 5S; (**d**): 7S.

Table 2. Physical and Mechanical Properties of the Developed Cellular Glass-Ceramics (5S, 6S, and 7S: fly ash-derived materials; RM: red mud-derived material).

Property	5S			6S			7S			RM
Firing temperature (°C)	800	900	1000	800	900	1000	800	900	1000	800
Density (g/cm^3)	0.51 ± 0.01	0.54 ± 0.01	0.81 ± 0.01	0.52 ± 0.01	0.54 ± 0.01	0.78 ± 0.01	0.61 ± 0.01	0.67 ± 0.01	0.94 ± 0.01	1.18 ± 0.04
Total porosity (vol%)	80 ± 2	81 ± 2	69 ± 1	80 ± 2	81 ± 2	70 ± 1	77 ± 6	76 ± 5	64 ± 1	65 ± 1
Open porosity (vol%)	79 ± 2	78 ± 2	68 ± 1	78 ± 2	77 ± 2	68 ± 1	76 ± 5	73 ± 2	62 ± 1	64 ± 1
Compressive strength (MPa)	0.2 ± 0.1	0.5 ± 0.1	3.2 ± 0.3	1.0 ± 0.1	1.2 ± 0.1	2.4 ± 0.1	1.0 ± 0.1	1.8 ± 0.3	6.0 ± 0.4	4.8 ± 0.6

The direct comparison of crushing strength data for porous bodies is not strictly appropriate, owing to the variability of porosity. In order to highlight differences resulting from other factors, the strength and density data were computed according to the well-known Gibson and Ashby model [17]. The model predicts the crushing strength (σ_c) as a function of the bending strength of the solid phase (σ_{bend}) and relative density (ρ_{rel}, defined as $\rho_{rel} = 1 - P/100$, where P is the total porosity) in the hypothesis of open-celled bodies as follows:
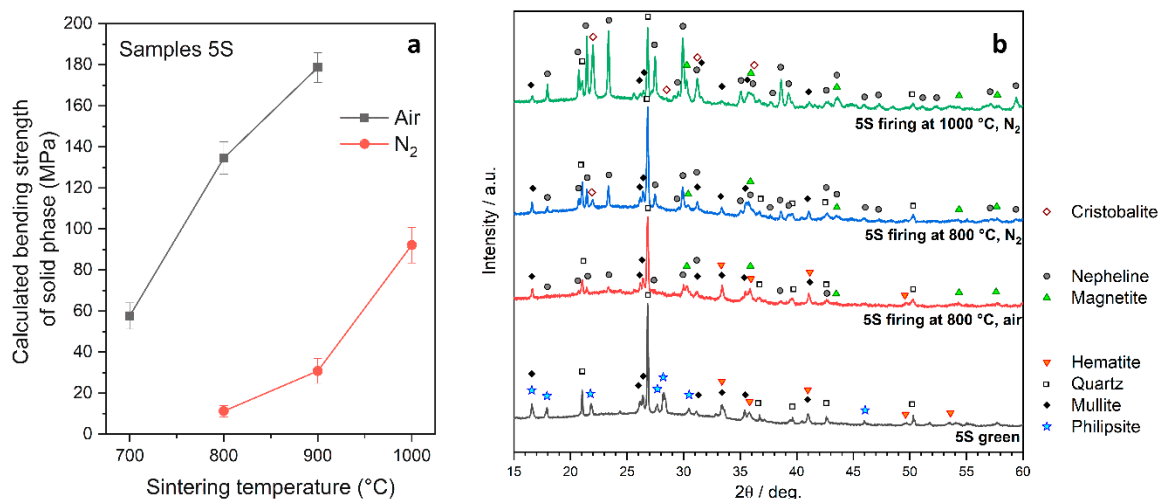
$$\sigma_c \approx \sigma_{bend} \cdot 0.2 \cdot (\rho_{rel})^{3/2} \tag{1}$$

Figure 2a, for the 5S sample, designed for the lowest SiO_2/Al_2O_3 nominal molar ratio ($SiO_2/Al_2O_3 = 5$, according to the highest content of FA), displays σ_{bend} values obtained from the

experimental data reported in Table 2, along with data from previous firing experiments in the air [15], by reversing Equation (1):

$$\sigma_{bend} \approx \sigma_c \cdot 5 \cdot (\rho_{rel})^{-3/2} \tag{2}$$

Figure 2. (**a**) Comparison of calculated bending strength of 5S samples fired in the air [15] and in N_2; (**b**) mineralogical analysis of selected 5S samples according to thermal treatment.

The values for 5S samples fired in N_2 remained far lower than those of analogous samples fired in air, except for treatments at 1000 °C. It should be noted that the calculated σ_{bend} values cannot be considered as an expression of the real strength of the solid phase in foams since the model neglects the stress concentration at pores, but they can highlight other microstructural contributions such as differences in phase assemblage, in turn causing internal stresses, arising from different FA/SLG interactions.

The products of the firing of FA/SLG gels could be seen as examples of glass-ceramics from direct sintering, not deriving from the conversion of a homogeneous glass, but relying on the reaction between a liquid phase—from softened waste glasses and several oxides and from other inorganic waste—with formation of silicate and alumino-silicate crystals [18]. In the 'green' state (Figure 2b), as observed in the previous investigation, foams contained quartz (SiO_2, PDF#083-0539), mullite (Al_4SiO_8, PDF#079-1275) and some minor hematite (Fe_2O_3, PDF#033-0664) traces—from the original fly ash [15] coupled with philipsite ($Na_4KAl_5Si_{11}O_{32}(H_2O)_{10}$, PDF#073-1419)—formed upon alkali activation [15]. The firing treatment at 800 °C determined some dissolution of quartz, in the liquid phase offered by SLG, and the development of nepheline ($Na_{6.65}Al_{6.24}Si_{9.76}O_{32}$, PDF#083-2372). The latter phase was confirmed with the increase of firing temperature up to 1000 °C, accompanied by cristobalite (SiO_2, PDF#082-0512). Iron oxide had significant evolution, passing from hematite to magnetite (Fe_3O_4, PDF#89-0691).

Figure 2b actually testifies that at the same temperature (800 °C), the firing in N_2 compared to that in air reduced the dissolution of quartz in softened SLG, with obvious consequences for strength. Quartz, in fact, is known to promote internal stresses upon cooling from the firing temperature according to the characteristic β → α transition, implying significant volume changes [19].

It is interesting to note that with the firing in N_2, nepheline had an opposite trend compared to quartz, given the intensity of diffraction peaks. The different atmosphere actually promoted the crystallization of the specific phase, probably due to the observed evolution of iron oxide. An enhanced the Fe^{2+}/Fe^{3+} redox ratio, besides favoring magnetite instead of hematite, is known to lower the activation energy for nepheline crystallization in alkali alumino-silicate glasses [20]. In the absence of a homogeneous parent glass, magnetite reasonably stimulated the transformation in nepheline of the (hydrated) alkali alumino-silicate gel (comprising philipsite) formed upon activation by ash/glass interaction.

The formation of nepheline was interesting also for its distinctive crystal structure, i.e., for the formation of a silica-based network with AlO_4 units—partially replacing SiO_4 units—nominally stabilized only by Na^+ ions but practically featuring many others in solid solution [21]. Iron ions can be incorporated in both Fe^{2+} and Fe^{3+} forms, along with K^+, Mg^{2+}, Mn^{2+}, and Ti^{4+}. 800 °C is actually recognized as the temperature of maximum solubility of $NaFeSiO_4$ (hypothetical pure 'iron nepheline', featuring Fe^{3+} ions) in $NaAlSiO_4$ (pure nepheline) [22]. Onuma et al. [23] even proposed the formation of $NaAlSiO_4/NaFeSiO_4/SiO_2$ solid solutions ($Na_{x+y}\square_{8-x-y}Al_xFe_ySi_{16-x-y}O_{32}$, where $\square$ represents a vacant site).

The 5S samples fired at 800 °C, although not acceptable due to their low strength, were quite interesting for the stabilization of pollutants. Table 3 clearly shows that the new firing conditions reduced the leaching of heavy metals, compared to the previous samples fired in air. The previously prepared 5S samples featured Mo slightly above the threshold for inert materials; in addition, the release of Cr, although below the threshold, was substantial. The firing in nitrogen kept Mo below the threshold and reduced dramatically the Cr leaching (marked in bold in Table 3).

Table 3. Leachate Chemical Analysis of Selected Samples Fired at 800°C. Bold: highlighted pollutants; Italic: reference data for previously developed samples fired in air.

| Element	Leachates (ppm)							Limits (ppm)	
	5S		6S		7S		RM		
	Air [15]	N_2	*Air* [15]	N_2	*Air* [15]	N_2	N_2	Inert	Non-Hazardous
As	*0.0316*	0.0061	*0.068*	0.0521	*0.0491*	0.0475	0.4876	0.5	2
Ba	*>Al*	<0.000	*>Al*	<0.000	*0.0672*	<0.000	0.0131	20	100
Cd	*<0.0002*	<0.0002	*<0.0002*	<0.0002	*<0.0002*	<0.0002	<0.0002	0.04	1
Cr	***0.3406***	**0.0008**	*0.0255*	**0.0004**	*0.0689*	**0.0009**	0.0303	0.5	10
Cu	*0.0029*	0.0048	*0.0024*	0.0023	*0.0053*	0.0034	0.0579	2	50
Hg	*0.0032*	<0.0004	*0.0006*	<0.0004	*0.0020*	<0.0004	<0.0004	0.01	0.2
Mo	***0.5324***	**0.4542**	*0.2107*	**0.0158**	*0.1973*	**0.4925**	0.0188	**0.5**	10
Ni	*<0.0014*	<0.0014	*<0.0014*	<0.0014	*<0.0014*	<0.0014	0.0146	0.4	10
Pb	*<0.0047*	<0.0047	*<0.0047*	<0.0047	*<0.0047*	<0.0047	0.0084	0.5	10
Se	*0.0133*	0.0168	*0.0255*	0.0194	*0.0226*	0.0177	0.0362	0.1	0.5
Zn	*<0.0203*	<0.0203	*<0.0203*	<0.0203	*<0.0203*	<0.0203	<0.0203	4	50

3.2. Effect of Glass Content on Microstructure and Properties of Fly Ash-Derived Glass-Ceramic Foams

Samples with increased SLG content, i.e., 6S and 7S, as shown by Figure 3a, remained still quite weak compared to samples fired in air but had a remarkable improvement in σ_{bend} compared to 5S (after firing at 800 °C), consistently with enhanced nepheline crystallization and quartz solubilization (see Figure 3b). In addition, they maintained the stabilization of pollutants, as reported by Table 3. The interpretation of the durability of a glass-ceramic is not straightforward, since stable crystals may be embedded in a poorly durable matrix or vice versa. Nepheline crystallization (stimulated by Fe), as an example, is generally seen as negative in nuclear glasses, not directly, but as the condition for the formation of a residual glass phase with poor durability [24]. In the present case, in our opinion, it had a positive impact in immobilizing alkali ions.

Alkali ions in glasses are known to reduce the durability but also to enhance the electrical conductivity, according to an ionic mechanism [25]. Quite surprisingly, all glass-ceramic samples fired at 800 °C exhibited a low electrical resistivity (ρ_{el}), passing from 2.7 $\Omega\cdot$m (5S) to 2.2 $\Omega\cdot$m (6S) and 0.9 $\Omega\cdot$m (7S), as shown by Figure 4a. In other words, the samples exhibited an electrical conductivity ($\sigma_{el} = 1/\rho_{el}$) up to 1.1 S/m, i.e., in the range of that of semiconductors [26]. Again, the presence of different phases is a great complication, but an explanation may come from the abovementioned inclusion of both Fe^{2+} and Fe^{3+} ions in nepheline. The electronic exchange between Fe^{2+} and Fe^{3+} sites ('electron hopping'), well documented for magnetite [27,28], likely occurred also in Fe-containing nepheline. The incorporation of both Fe^{2+} and Fe^{3+} in nepheline and in the residual glass phase may

be supported by the fact magnetite was actually more visible in the diffraction pattern of the 7S sample (Figure 3b), although less Fe_2O_3-rich, i.e., deriving from a lower content of FA.

Figure 5 shows results from scanning electron microscopy analysis applied on samples fired at 800 °C. The homogeneity of foams already observed by means of optical microscopy was confirmed by the low magnification backscattered electrons images of 5S (Figure 5a) and 7S (Figure 5b) samples. The lighter 'spots' suggested the concentration of heavier elements such as Fe. However, it must be noted that there was no neat separation of iron oxide particles; iron was found in clusters (center of Figure 5c; arrows marked in Figure 5d) accompanied by other elements (Na, Al, Si, as found in nepheline, but also Mg) as well in the darker matrix (see energy dispersive X-ray spectrum in Figure 5e). High magnification images actually provided a further justification of the strength enhancement of samples fired at 800 °C, with increasing glass content: the enhanced viscous flow promoted the formation of necks between adjacent particles (7S sample, in Figure 5d), less visible in sample with lower soda-lime content (5S sample, in Figure 5c).
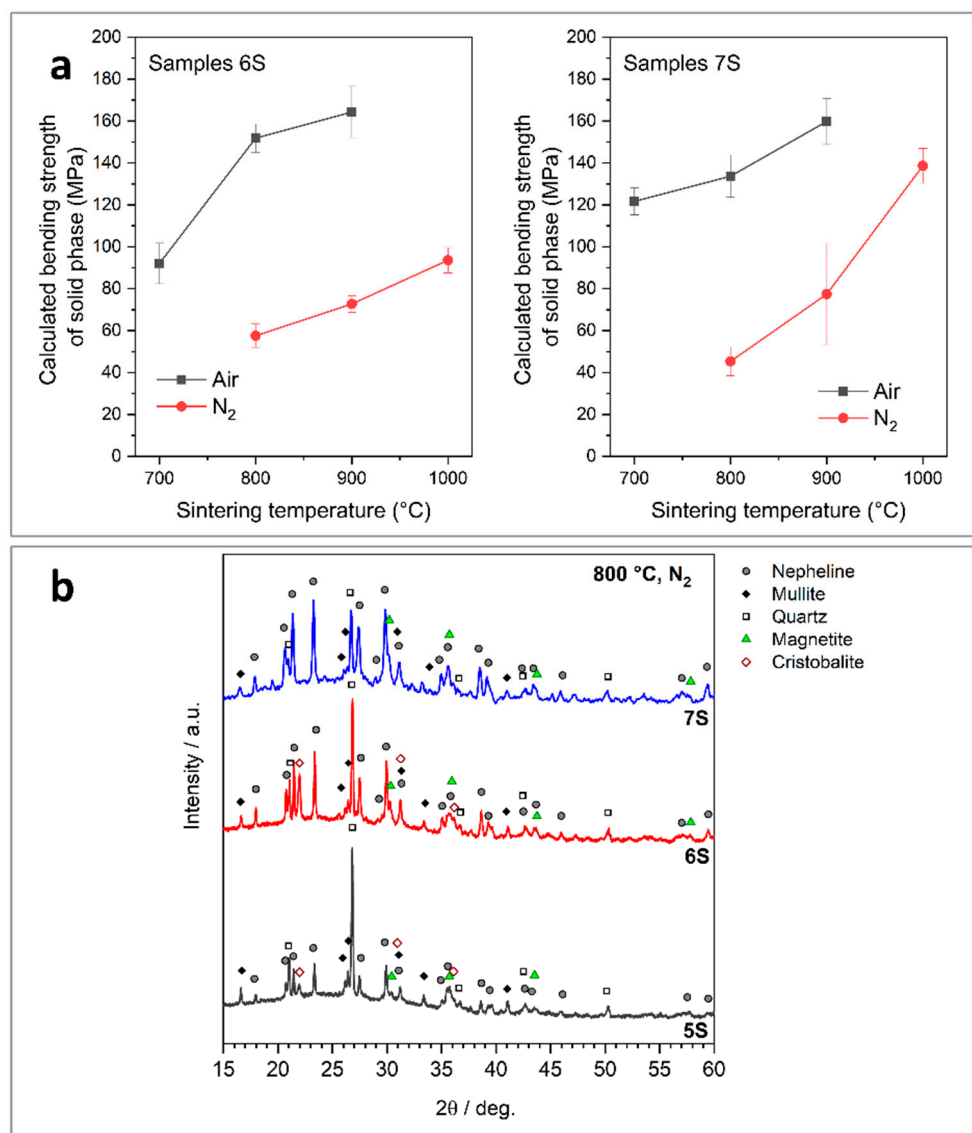
Figure 3. (**a**) Comparison of calculated bending strength of 6S and 7S samples fired in air [15] and in N_2; (**b**) evolution of phase assemblage, after firing at 800 °C (in N_2) according to reduction of the fly ash from coal combustion (FA)/glass ratio.
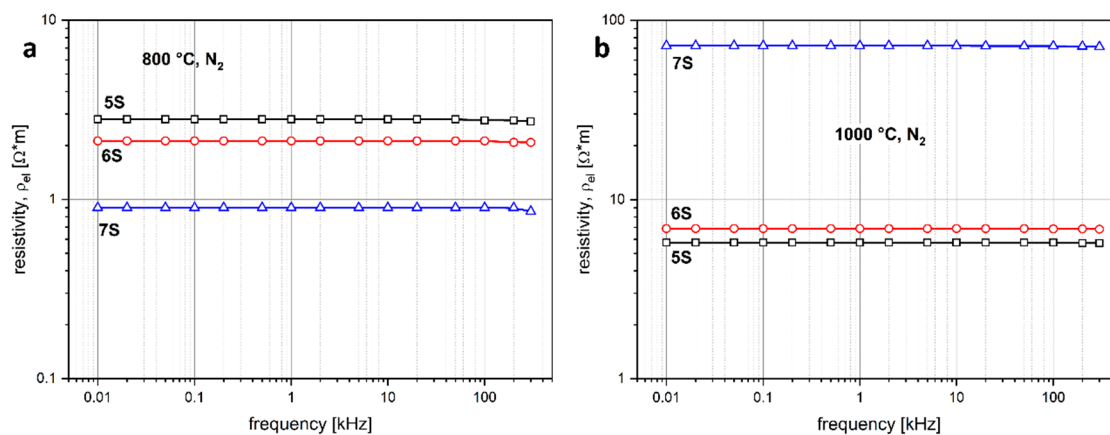
**Figure 4.** Electrical resistivity of FA/glass samples fired in nitrogen at 800 °C (**a**) and 1000 °C (**b**).
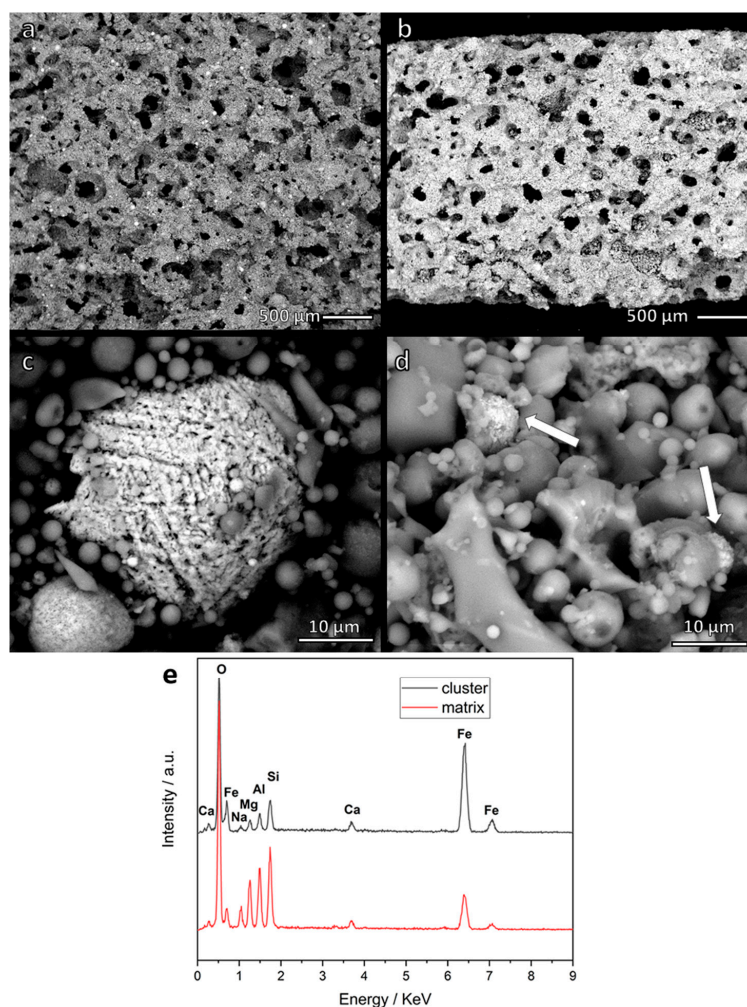
Figure 5. Scanning electron microscopy analysis of samples fired at 800 °C: (**a**,**c**) 5S; (**b**,**d**) 7S (iron-rich clusters marked by arrows); (**e**) analysis of Fe-rich cluster and matrix in 5S sample.

The electrical conductivity (coupled with chemical stability) of foams fired at 800 °C may open the way for the application of waste-derived materials even well beyond thermal and acoustic insulation, without modifications (such as application of conducting coatings) as electrocatalysts [29] or even porous anodes for microbial fuel cells [30].

3.3. Effect of Firing Temperature on Microstructure and Properties of Fly Ash-Derived Glass-Ceramic Foams

As shown by Figure 3a, an increase in the firing temperature up to 1000 °C in nitrogen was necessary to obtain stronger foams. At 1000 °C, in fact, the viscous flow of the glass component was evidently favored; according to Figures 2b and 6a, a more substantial reduction of quartz, accompanied by enhanced nepheline crystallization occurred. However, cristobalite formed as additional silica polymorph for samples 5S and 6S. The quite limited σ_{bend} could be interpreted again as an effect of internal stresses, from cristobalite $\beta \rightarrow \alpha$ transition [31]; the glass-ceramic sample 7S, not including cristobalite, had a far higher σ_{bend} (nearly 140 MPa). The latter value matches well with the bending strength of waste-derived glass-ceramics [15].
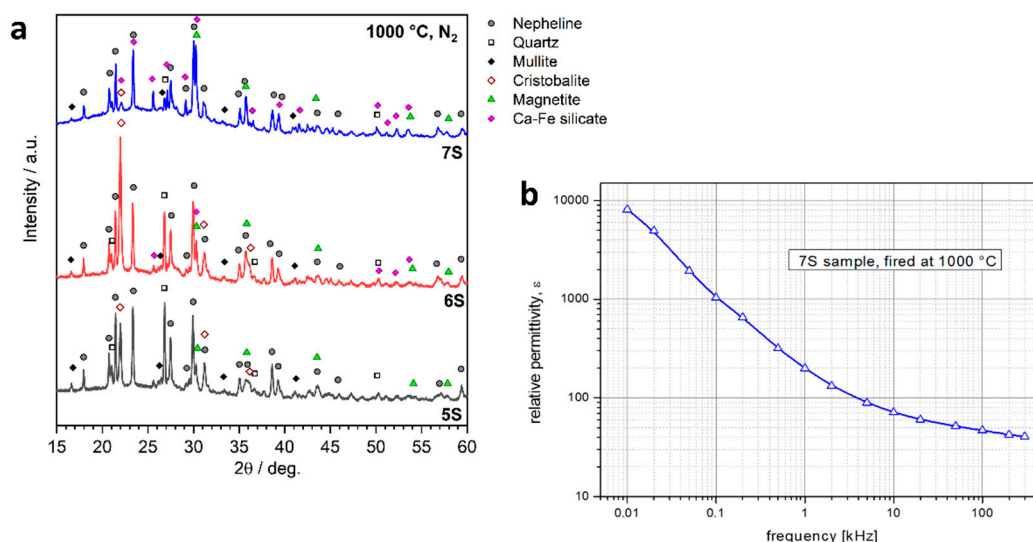

Figure 6. (**a**) Evolution of phase assemblage, after firing at 800 °C (in N_2) according to reduction of FA/glass ratio; (**b**) permittivity/frequency plot for 7S sample.

The mineralogical analysis in Figure 6a is significant in evidencing a clear separation of iron oxide as magnetite. Interestingly, Fe_3O_4 emerged more neatly again in the 7S sample, possessing the lowest nominal iron content and also featuring the formation of an extra iron-containing phase, such as Ca-Fe silicate (hedenbegite, $CaFe(Si_2O_6)$, PDF#87-1698). The sample exhibited a far higher resistivity than in the previous cases (>70 $\Omega\cdot$m) according to Figure 4b. The same figure actually illustrates an inversion of the ranking in resistivity, passing from 800 to 1000 °C (the less resistive after firing at 800 °C turned into the most resistive at 1000 °C). The concentration of iron ions in magnetite and hedenbergite, reasonably stimulated by an easier ionic interdiffusion in more liquid phase from softened SLG, evidently determined an insulating matrix, featuring 'purer' (i.e., not iron-doped) nepheline. With 5S and 6S, the resistivity remained quite low (5.7 $\Omega\cdot$m for 5S, 6.9 $\Omega\cdot$m for 6S) as an effect of Fe^{2+}/Fe^{3+} ions outside magnetite.

The analysis of samples fired at 1000 °C by scanning electron microscopy, shown in Figure 7, provided a substantial confirmation of the mineralogical analysis. The foams kept high homogeneity, although the enhanced viscous flow determined the 'reshaping' of the cellular structures (Figure 7a,b, for 5S and 7S samples, respectively). High magnification details evidenced the formation of a multitude of tiny iron-rich inclusions (even below 1 μm), more abundant for 7S sample (see Figure 7c,d, for 5S and 7S samples, respectively).

The dispersion of tiny conducting particles in an insulating matrix [32] is recognized as a fundamental strategy for achieving materials with huge permittivity, i.e., a particularly remarkable electric polarization. In other words, the more resistive 7S sample, when fired at 1000 °C, could bring additional opportunities. As illustrated by Figure 6b, the sample was actually comparable to highly

polarizable dielectrics, with relative permittivity approaching the huge value of 9000, at low frequency, and remaining above 200 up to 1 kHz.
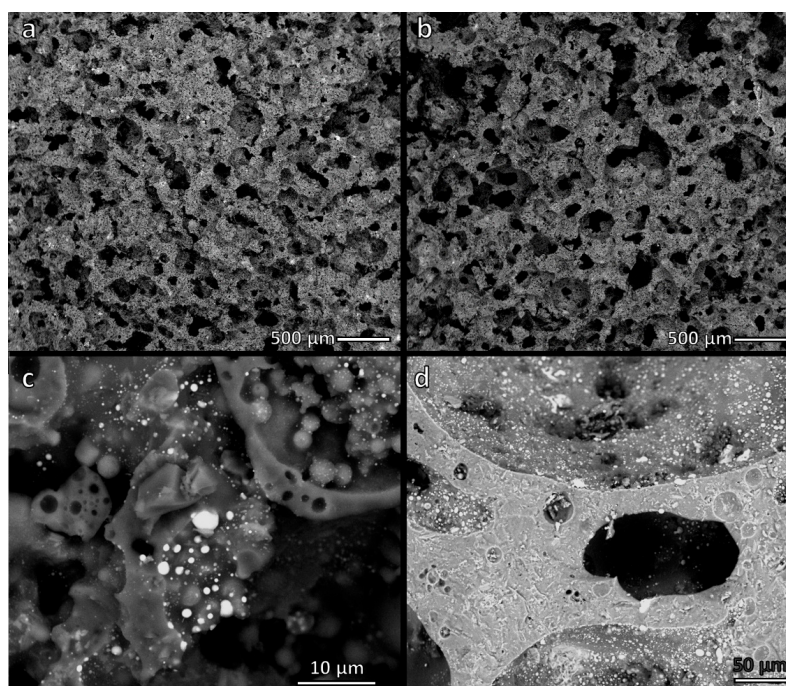
Figure 7. Scanning electron microscopy analysis of samples fired at 1000 °C: (**a**,**c**) 5S; (**b**,**d**) 7S.

The frequency sensitivity of permittivity is interpreted as an effect of the trapping of hopping electrons in the dispersed phase [26] at low frequency; higher frequencies 'unlock' the electron exchanges across the interfaces. In addition, for the firing at 1000 °C, the new functionality may extend the applications of waste-derived foams in novel electrical devices. As an example, the materials could provide an alternative to $PrCrO_3$ semiconductor ceramics relaxor ferroelectric-like giant permittivity, as presented by Prasad et al. [33]. It should be noted that the safety of the developed materials, with firing temperature increased up to 1000 °C, was not compromised. Table 4 confirms the stabilization of pollutants; Mo leaching, in particular, was kept well below the limits.

Table 4. Leachate Chemical Analysis of Selected Samples Fired at 1000 °C (in N_2). Bold: highlighted pollutants; Italic: reference data for previously developed samples fired in air.

| Element	Leachates (ppm)						Limits (ppm)	
	5S		6S		7S			
	800 °C	1000 °C	800 °C	1000 °C	800 °C	1000 °C	Inert	Non-Hazardous
As	0.0061	<0.0049	0.0521	0.0521	0.0475	0.0188	0.5	2
Ba	<0.000	0.0028	<0.000	<0.000	<0.000	<0.000	20	100
Cd	<0.0002	<0.0002	<0.0002	<0.0002	<0.0002	<0.0002	0.04	1
Cr	*0.0008*	*0.0007*	*0.0004*	*0.0004*	*0.0009*	*0.0009*	0.5	10
Cu	0.0048	0.0074	0.0023	0.0054	0.0034	0.0072	2	50
Hg	<0.0004	<0.0004	<0.0004	<0.0004	<0.0004	<0.0004	0.01	0.2
Mo	*0.4542*	*0.0129*	*0.0158*	*<0.0033*	*0.4925*	*0.0735*	**0.5**	10
Ni	<0.0014	<0.0014	<0.0014	<0.0014	<0.0014	<0.0014	0.4	10
Pb	<0.0047	<0.0047	<0.0047	<0.0047	<0.0047	<0.0047	0.5	10
Se	0.0168	0.0187	0.0194	0.0230	0.0177	<0.0122	0.1	0.5
Zn	<0.0203	<0.0203	<0.0203	<0.0203	<0.0203	<0.0203	4	50

3.4. Extension of the Approach to Red Mud-Derived Glass-Ceramic Foams

The results with fly ash-based samples stimulated additional studies to confirm the observed coupling of stabilization and functionalization. Red mud was specifically considered for its high content of iron oxide to verify the role of magnetite. For the sake of simplicity, the waste/glass proportions were kept at 70/30 (wt.%).

Figure 8a (secondary electron image, evidencing morphological details) shows that although less homogeneous, foams could be achieved again by weak alkali activation, frothing, and sintering. In this case, 800 °C sufficed in determining strong porous glass-ceramics (compressive strength approaching 5 MPa, with a porosity of 65 vol%, see Table 1). Similarly to the 7S sample fired at 1000 °C, magnetite and nepheline constituted the main phases, as illustrated in Figure 9a, accompanied by hedenbergite and gehlenite ($CaAl_2SiO_7$, PDF#79-1726). The effectiveness of treatment in nitrogen in promoting Fe^{3+} reduction is evident from the fact that red mud, in the starting condition, featured Fe^{3+}-containing phases, such as hematite, Fe_2O_3, and goethite (FeO(OH), PDF#29-0713), accompanied by many other minor phases.

The coupling of stabilization and functionalization was still possible. As reported by Table 3, the sample (labelled as 'RM') was inert, with a dramatic decrease of the release of chromium (as received red mud, not shown in Table 3, led to a leaching of Cr exceeding 1 ppm). A huge dielectric permittivity was obtained at low frequencies (Figure 9b,c) but accompanied by a much higher resistivity (exceeding $7 \cdot 10^4$ $\Omega \cdot$m). The two electrical properties both decreased with increasing frequency. This behavior could be explained, in our opinion, as still based on the magnetite conductive inclusions, allowing a remarkable interfacial polarization which is relaxed at high frequency [34]. The lower maximum permittivity, compared to the 7S sample, could be caused by the different microstructure. As shown by Figure 8b (backscattered electron image, evidencing compositional gradients) magnetite was present in coarser particles (>100 μm), surrounded by quite wide iron-containing 'halos' (up to 1 mm wide).

A final remark may concern the reproducibility of the findings. Further work will be undoubtedly dedicated to the study of functional properties on the basis of a high number of samples, e.g., made starting from different batches of FA and RM. Adjustments in the glass/waste ratio may constitute a tool to overcome possible variations in the chemical composition.
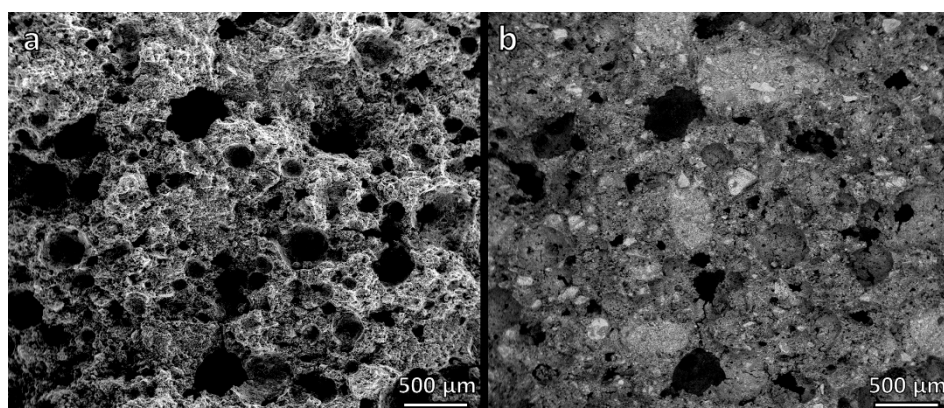
Figure 8. Red mud/glass-derived porous glass-ceramic: (**a**) morphology; (**b**) compositional gradients.
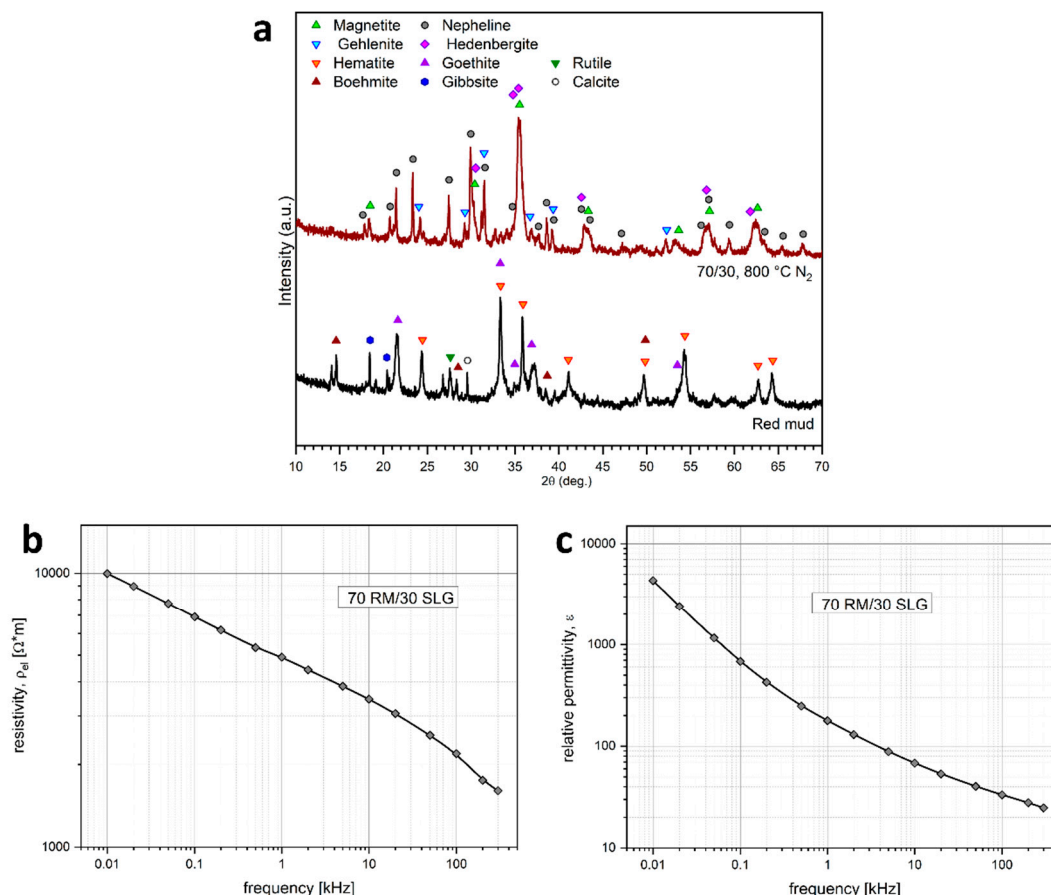
Figure 9. Characterization of RM-derived glass-ceramic foam (**a**) mineralogical analysis; (**b**) resistivity/frequency plot; (**c**) relative permittivity/frequency plot.

4. Conclusions

We may conclude that:

- The inclusion of fly ash (FA) powders mixed with soda-lime glass (SLG) waste in weakly alkaline solutions was confirmed as an excellent approach to produce glass-ceramic foams, allowing the incorporation of high proportions of fly ash.
- Gelation of FA/SLG suspensions was not a final stage, but it enabled the manufacturing of highly porous bodies by simple frothing.
- The decomposition of the gel and the SLG/FA interactions upon firing in N_2 promoted the formation of new phases, among which nepheline was dominant; such a phase was stimulated by the separation of iron oxide into magnetite phase, in turn favored by the adoption of an inert atmosphere.
- The modifications in the phase assemblage, promoted by treatments in nitrogen, favored the chemical stability of the glass-ceramics as assessed by means of leaching tests.
- Firing in nitrogen, compared to firing in air, generally led to mechanically weaker samples according to the modifications in phase assemblage at low temperature; however, treatments at 1000 °C led to foams with remarkable strength.
- Treatments in nitrogen atmosphere, although more expensive, bring advantages, besides in durability, in the development of electrical functionalities that could be tuned according to FA/SLG proportions and firing temperature. Semiconductive or highly polarizable foams could find applications in electrocatalysis and energy generation.

- The distribution of iron in the glass-ceramic and, in particular, its concentration in magnetite inclusions, controls the electrical functionality; the results from FA/SLG mixtures were substantially confirmed by additional glass-ceramic foams (still featuring nepheline) from red mud/SLG mixtures.

Author Contributions: For this paper, E.B., D.D. and A.R.B. formulated research ideas and supervised the experiments. A.R.R. and D.D. performed the general experimentation. E.B. and A.R.B. contributed to the discussion of results. A.R.R., D.D. and E.B. have written and edited the article. All authors have read and agreed to the published version of the manuscript.

Conflicts of Interest: The authors declare no conflict of interest.

References

1. Korhonen, J.; Nuur, C.; Feldmann, A.; Birkie, S.E. Circular economy as an essentially contested concept. *J. Clean. Prod.* **2018**, *175*, 544–552. [CrossRef]
2. Korhonen, J.; Honkasalo, A.; Seppälä, J. Circular Economy: The Concept and its Limitations. *Ecol. Econ.* **2018**, *143*, 37–46. [CrossRef]
3. Smol, M.; Kulczycka, J.; Henclik, A.; Gorazda, K.; Wzorek, Z. The possible use of sewage sludge ash (SSA) in the construction industry as a way towards a circular economy. *J. Clean. Prod.* **2015**, *95*, 45–54. [CrossRef]
4. Yao, Z.T.; Ji, X.S.; Sarker, P.K.; Tang, J.H.; Ge, L.Q.; Xia, M.S.; Xi, Y.Q. A comprehensive review on the applications of coal fly ash. *Earth-Sci. Rev.* **2015**, *141*, 105–121. [CrossRef]
5. Lima, M.S.S.; Thives, L.P.; Haritonovs, V.; Bajars, K. Red mud application in construction industry: Review of benefits and possibilities. In *IOP Conference Series: Materials Science and Engineering*; IOP Publishing: Bristol, UK, 2017; Volume 251, p. 012033.
6. Al Bakri, M.M.; Mohammed, H.; Kamarudin, H.; Khairul Niza, I.; Zarina, Y. Review on fly ash-based geopolymer concrete without Portland Cement. *J. Eng. Technol. Res.* **2011**, *3*, 1–4.
7. Dimas, D.D.; Giannopoulou, I.P.; Panias, D. Utilization of alumina red mud for synthesis of inorganic polymeric materials. *Min. Proc. Extr. Met. Rev.* **2009**, *30*, 211–239. [CrossRef]
8. Toniolo, N.; Boccaccini, A.R. Fly ash-based geopolymers containing added silicate waste. A review. *Ceram. Int.* **2017**, *43*, 14545–14551. [CrossRef]
9. Provis, J.L. Geopolymers and other alkali activated materials: Why, how, and what? *Mater. Struct.* **2014**, *47*, 11–25. [CrossRef]
10. Tchakouté, H.K.; Rüscher, C.H.; Kong, S.; Kamseu, E.; Leonelli, C. Geopolymer binders from metakaolin using sodium waterglass from waste glass and rice husk ash as alternative activators: A comparative study. *Const. Build. Mat.* **2016**, *114*, 276–289. [CrossRef]
11. Toniolo, N.; Rincón, A.; Roether, J.A.; Ercole, P.; Bernardo, E.; Boccaccini, A.R. Extensive reuse of soda-lime waste glass in fly ash-based geopolymers. *Const. Build. Mat.* **2018**, *188*, 1077–1084. [CrossRef]
12. Toniolo, N.; Rincón, A.; Avadhut, Y.S.; Hartmann, M.; Bernardo, E.; Boccaccini, A.R. Novel geopolymers incorporating red mud and waste glass cullet. *Mater. Lett.* **2018**, *219*, 152–154.
13. Toniolo, N.; Taveri, G.; Hurle, K.; Roether, J.A.; Ercole, P.; Dlouhy, I.; Boccaccini, A.R. Fly-Ash-Based Geopolymers: How the Addition of Recycled Glass or Red Mud Waste Influences the Structural and Mechanical Properties. *J. Ceram. Sci. Technol.* **2017**, *8*, 411–420.
14. Idir, R.; Cyr, M.; Pavoine, A. Investigations on the durability of alkali-activated recycled glass. *Const. Build. Mat.* **2020**, *235*, 117477.
15. Rincón Romero, A.; Toniolo, N.; Boccaccini, A.R.; Bernardo, E. Glass-Ceramic Foams from 'Weak Alkali Activation' and Gel-Casting of Waste Glass/Fly Ash Mixtures. *Materials* **2019**, *12*, 588.

16. Rabelo Monich, P.; Rincón Romero, A.; Desideri, D.; Bernardo, E. Waste-derived glass-ceramics fired in nitrogen: Stabilization and functionalization. *Const. Build. Mat.* **2020**, *232*, 117265.

17. Gibson, L.J.; Ashby, M.F. *Cellular Solids: Structure and Properties*, 2nd ed.; Cambridge University Press: Cambridge, UK, 2014; pp. 1–510.

18. Cetin, S.; Marangoni, M.; Bernardo, E. Lightweight glass-ceramic tiles from the sintering of mining tailings. *Ceram. Int.* **2015**, *41*, 5294–5300.

19. Chmelík, F.; Trník, A.; Štubňa, I.; Pešička, J. Creation of microcracks in porcelain during firing. *J. Eur. Ceram. Soc.* **2011**, *31*, 2205–2209.

20. Shaharyar, Y.; Cheng, J.Y.; Han, E.; Maron, A.; Weaver, J.; Marcial, J.; McCloy, J.S.; Goel, A. Elucidating the Effect of Iron Speciation (Fe^{2+}/Fe^{3+}) on Crystallization Kinetics of Sodium Aluminosilicate Glasses. *J. Am. Ceram. Soc.* **2016**, *99*, 2306–2315.

21. Duke, D.A.; MacDowell, J.F.; Karstetter, B.R. Crystallization and Chemical Strengthening of Nepheline Glass-Ceramics. *J. Am. Ceram. Soc.* **1967**, *50*, 67–74.

22. Ahmadzadeh, M.; Marcial, J.; McCloy, J.S. Crystallization of iron-containing sodium aluminosilicate glasses in the $NaAlSiO_4$-$NaFeSiO_4$ join. *JGR Solid Earth* **2017**, *122*, 2504–2524.

23. Onuma, K.; Iwai, T.; Yagi, K. Nepheline-"Iron-Nepheline" Solid Solutions. *J. Fac. Sci. Hokkaido Univ.* **1972**, *15*, 179–190.

24. Sargin, I.; Lonergan, C.E.; Vienna, J.D.; McCloy, J.S.; Beckman, S.P. A data-driven approach for predicting nepheline crystallization in high-level waste glasses. *J. Am. Ceram. Soc.* **2020**, *103*, 4913–4924. [CrossRef]

25. Ezz Eldin, F.M.; El Alaily, N.A. Electrical conductivity of some alkali silicate glasses. *Mat. Chem. Phys.* **1998**, *52*, 175–179. [CrossRef]

26. Abdullah, M.H.; Yusoff, A.N. Complex impedance and dielectric properties of an Mg-Zn ferrite. *J. Alloys Compd.* **1996**, *233*, 129–135. [CrossRef]

27. Gillot, B.; Bouton, F.; Chassagneux, F.; Rousset, A. Electrical conductivity of ($Fe^{2+}Al_{2-x}^{3+}Cr_x^{3+}$)$O_4^{2-}$ spinels and defect phases γ($Fe_{1/3}^{3+}Al_{2/3-y}^{3+}Cr_y^{3+}$)$_2O_3^{2-}$. *Phys. St. Sol.* **1978**, *50*, 109–116. [CrossRef]

28. Sastry, M.D.; Nagar, Y.C.; Bhushan, B.; Mishra, K.P.; Balaram, V.; Singhvi, A.K. An unusual radiation dose dependent EPR line at g_{eff} = 2.54 in feldspars: Possible evidence of $Fe^{3+}O^{2-}$ ↔ $Fe^{2+}O^-$ and exchange coupled Fe^{3+}–Fe^{2+}–nO^-. *J. Phys. Cond. Mat.* **2007**, *20*, 025224.

29. Li, W.-H.; Lv, J.; Li, Q.; Xie, J.; Ogiwara, N.; Huang, Y.; Jiang, H.; Kitagawa, H.; Xu, G.; Wang, Y. Conductive metal–organic framework nanowire arrays for electrocatalytic oxygen evolution. *J. Mater. Chem. A* **2019**, *7*, 10431. [CrossRef]

30. Canuto de Almeida e Silva, T.; Bhowmick, G.D.; Ghangrekar, M.M.; Wilhelm, M.; Rezwan, K. SiOC-based polymer derived-ceramic porous anodes for microbial fuel cells. *Biochem. Eng. J.* **2019**, *148*, 29–36. [CrossRef]

31. Breneman, R.C.; Halloran, J.W. Effect of Cristobalite on the Strength of Sintered Fused Silica Above and Below the Cristobalite Transformation. *J. Am. Ceram. Soc.* **2015**, *98*, 1611–1617. [CrossRef]

32. Li, Y.; Huang, X.; Hu, Z.; Jiang, P.; Li, S.; Tanaka, T. Large Dielectric Constant and High Thermal Conductivity in Poly (vinylidene fluoride)/Barium Titanate/Silicon Carbide Three-Phase Nanocomposites. *ACS Appl. Mater. Interfaces* **2011**, *3*, 4396–4403. [CrossRef]

33. Prasad, B.V.; Rao, G.N.; Chen, J.W.; Babu, D.S. Relaxor ferroelectric like giant permittivity in $PrCrO_3$ semiconductor ceramics. *Mat. Chem. Phys.* **2011**, *126*, 918–921. [CrossRef]

34. Jonscher, A.K. Dielectric relaxation in solids. *J. Phys. D Appl. Phys.* **1999**, *32*, R57. [CrossRef]